ADVANCED FUNCTIONAL MATERIALS
www.afm-journal.de

Biochemical Gradients to Generate 3D Heterotypic-Like Tissues with Isotropic and Anisotropic Architectures

Raphaël F. Canadas, Tanchen Ren, Alexandra P. Marques, Joaquim M. Oliveira, Rui L. Reis, and Utkan Demirci**

Anisotropic 3D tissue interfaces with functional gradients found in nature are replicated in vitro for drug development and tissue engineering. Even though different fabrication techniques, based on material science engineering and microfluidics, are used to generate such microenvironments, mimicking the native tissue gradient is still a challenge. Here, the fabrication of 3D structures are described with linear/random porosity and gradient distribution of hydroxyapatite microparticles which are combined with a gradient of growth factors generated by a dual chamber for the development of heterotypic-like tissues. The hydroxyapatite gradient is formed by applying a thermal ramp from the first to the second gel layer, and the porous architecture is controlled through ice templating. A 3D osteochondral (OC) tissue model is developed by codifferentiating fat pad adipose-derived stem cells. Osteogenic and chondrogenic markers expression is spatially controlled, as it occurs in the native osteochondral unit. Additionally, a prevasculature is spatially induced by the perfusion of proangiogenic medium in the bone-like region, as observed in the native subchondral bone. Thus, in this study, precise spatial control is developed over cell/tissue phenotype and formation of prevasculature which opens up possibilities for the study of complex tissues interfaces, with broader applications in drug testing and regenerative medicine.

1. Introduction

Anisotropic gradient structures present in living systems are the result of millions of years of evolution through natural selection, which led to optimized heterotypic tissues and organs.[1] In native tissues, interfaces are presented with spatiotemporal patterns, including variation in both cell types and extracellular matrix (ECM).[2] Gradients of bioactive signaling molecules are known to lead tissue formation and regeneration, as it is observed in embryonic development, aging, and even in degenerative diseases.[2–4] Moreover, oriented architectures of cellular and ECM also accompany the biochemical gradients in native hierarchical tissues. Interfaces, layers and columns are characteristics of the bone-to-soft tissue transitions,[5–7] or even the skin[8] and cortex[9] organizations, among others.[10–12] Particularly, the osteochondral (OC) interface is an example of a hierarchical tissue.[13,14] The OC unit presents a gradient of calcified ECM from subchondral bone to cartilage, along with a decrease in the tissue's vascularity. Furthermore, OC tissue is also characterized by the specific anisotropic orientation of the subchondral bone and calcified cartilage region. These spatial patterns are important regulators of cell adhesion, proliferation, migration, and differentiation.[2] Strikingly, none of these features have been addressed together when trying to mimic tissue interfaces in vitro.

Guided porous architectures and gradients are important to control 3D cell distribution and phenotype, and therefore, for the improvement of the biological function of the construct.[15] Recently, biomimetic and spatially tailored

R. F. Canadas, A. P. Marques, J. M. Oliveira, R. L. Reis
3B's Research Group
I3Bs—Research Institute on Biomaterials
Biodegradables and Biomimetics
University of Minho
Headquarters of the European Institute of Excellence on Tissue Engineering and Regenerative Medicine
AvePark, Parque de Ciência e Tecnologia
Zona Industrial da Gandra
4805-017 Barco, Guimarães, Portugal
E-mail: rgreis@i3bs.uminho.pt

R. F. Canadas, A. P. Marques, J. M. Oliveira, R. L. Reis
ICVS/3B's—PT Government Associate Laboratory
4806-909 Braga/Guimarães, Portugal

The ORCID identification number(s) for the author(s) of this article can be found under https://doi.org/10.1002/adfm.201804148.

DOI: 10.1002/adfm.201804148

R. F. Canadas, T. Ren, U. Demirci
Bio-Acoustic MEMS in Medicine (BAMM) Laboratory
Canary Center at Stanford for Cancer Early Detection
Department of Radiology
Stanford School of Medicine
Palo Alto, CA 94304, USA
E-mail: utkan@stanford.edu

A. P. Marques, J. M. Oliveira, R. L. Reis
The Discoveries Centre for Regenerative and Precision Medicine
Headquarters at University of Minho
Avepark 4805-017, Barco, Guimarães, Portugal

U. Demirci
Electrical Engineering Department
Stanford University
Stanford, CA 94305, USA

microenvironments have been synthesized in 3D structures. Current methods have been developed to create structural,[16,17] mechanical,[18,19] or biochemical gradients,[20,21] relying on material science,[22] bioprinting,[7,23] microscale engineering,[24–27] and microfluidic techniques.[28] Although each of the previous methods can control 3D gradient formation, the combination of relevant architectures by porosity guidance with structural gradients has not been achieved. Moreover, these current strategies usually fail when applied in cultures of multicell types with localized control over phenotype, as required for heterotypic tissues and interfaces formation. Thus, the combination of spatially organized scaffolds composition, along with culturing multiple cell types with gradients of signaling molecules is extremely important.[29] Likewise, user-friendly techniques need to be developed and made accessible to a broad range of researchers, envisioning a scale-up when translated to industry for clinical availability.[30,31]

Here, we combined in 3D structures both microparticle gradients and guided porosity for the development of heterotypic tissues and interfaces. Methacrylated gelatin (GelMA) and gellan gum (gg) were selected to create the 3D structure because of their biological and mechanical characteristics, respectively, as previously demonstrated.[32] Convection streams induced by temperature differences in the mixing of two polymeric solutions were tested to create HAp gradients (**Figure 1**A). Crosslinking and freezing mechanisms were tuned to guide polymeric chains arrangement and ice crystals growth to obtain isotropic (Figure 1B) or anisotropic (Figure 1C) porous architectures. As a proof of concept, we applied 3D gradient structures with guided porosity to explore their impact on bone and cartilage simultaneous codifferentiation of fat pad adipose-derived stem cells (ASCs) using a dual-chamber bioreactor (Figure 1E). The localized expression of bone and cartilage markers were demonstrated. Moreover, marker expression and porous architecture were correlated showing their direct interdependence. Additionally, spatial control over prevasculature formation was further investigated. Overall, this study will offer a feasible approach toward generation of functional 3D OC tissues, with potential applications for broader heterotypic tissues and interfaces.

2. Results

To evaluate the architecture, composition, and porosity profiles of the 3D anisotropic and isotropic gradient structures, X-ray computed microtomography (micro-CT) reconstruction and analysis were performed showing the porosity orientation, either forming isotropic or anisotropic structure organizations (**Figure 2**A-i,ii). Moreover, the ceramic phase was composed of HAp which followed the porosity orientation, demonstrating the generation of specific bioactive microparticle distribution patterns. Quantitative data were graphically traced revealing the gradient of HAp (Figure 2B-i). The structure made of randomly oriented pores, therefore, isotropic structure, presented lower porosity percentages when compared to the anisotropic one (Figure 2B-ii). Further, the pore size formation was controlled to be lower than 200 µm (Figure 2B-iii). Additionally, while forming the 3D structures, it was possible to program the pore vertical or random orientation by vertically or randomly guiding ionic crosslinking and ice crystal growth, as demonstrated by the anisotropic degree of the porous architecture significantly increased (Figure 2B-iv). When this degree was closer to 1 (larger than 0.5), anisotropic porosity was formed in the structures, meaning that its pores were vertically aligned, while a degree closer to 0 (zero) represented isotropic porous structures, where a randomly organized porous architecture was formed. Strikingly, the structural gradient was maintained both in the fabricated anisotropic and isotropic porous structures (Figure 2B-i).

To macroscopically characterize the gradient of HAp, Alizarin red was used to stain the phosphate groups in HAp microparticles, the distribution profile was shown and quantified in the structure (**Figure 3**A-i,ii). Further, the incorporation of the microparticles in the polymeric walls of 2–4 µm was observed using scanning electron microscope (SEM) (Figure 3A-iii). The characteristic formulation of HAp was confirmed after the structure fabrication process, revealing the characteristic peaks of an amorphous HAp by X-ray diffraction (XRD, Figure S5A, Supporting Information). In addition, the Fourier transform infrared spectrometry (FTIR) showed a characteristic spectrum composed of peaks within wavelengths of the chemical groups PO_4^{3-}, OH, CO_3^{2-}, and HPO_4^{2-}, which are characteristic of nonstoichiometric HAp (Figure S5B, Supporting Information). PO_4^{3-} group formed intensive infrared absorption bands at 560 and 600 cm^{-1} and from 1000 to 1100 cm^{-1}. The CO_3^{2-} group intensive peaks between 1460 and 1530 cm^{-1} were also present, showing that HAp kept incorporated after structure's fabrication, conferring its natural bioactive characteristics (Figure S5B-i, Supporting Information). The deposition of phosphorus (P) and calcium (Ca) increased over 14 d increased in the richest regions of the gradient in simulated body fluid (SBF), which demonstrated the bioactivity inherent to the fabricated structures by energy-dispersive X-ray spectrometry (Figure 3B-ii).

Mechanical properties of isotropic and anisotropic porous structures, using dynamic mechanical analysis (DMA), were compared regarding their storage modulus and loss factor (Figure 3C). A decrease in storage modulus (E') was registered while a constant range of values was observed for the anisotropic and isotropic porous structures, respectively (Figure 3C-i). The absolute value of *E*' was lower for the isotropic porous structures than the anisotropic ones (about twofold decreased), meaning that these structures presented higher deformability. Assessing the tan δ (Figure 3C-ii), the isotropic porous structures presented higher absolute value (about twofold increased), showing lower difference between the storage modulus and the loss factor. Thus, the isotropic porous structures presented higher ability to dissipate energy, under dynamic load in a range from 0 to 10 Hz frequency, thus being more viscous and less prone to mechanical deformation.

To test the formation of a gradient environment, the histogram of two different dyes perfusing the dual-chamber bioreactor was traced (**Figure 4**A). The mixing profile of blue and red dyes showed a color gradient at the interface characterized by the formation of a yellow region (Figure 4A-i). To mimic a native gradient tissue, OC phenotype was selected as a model.

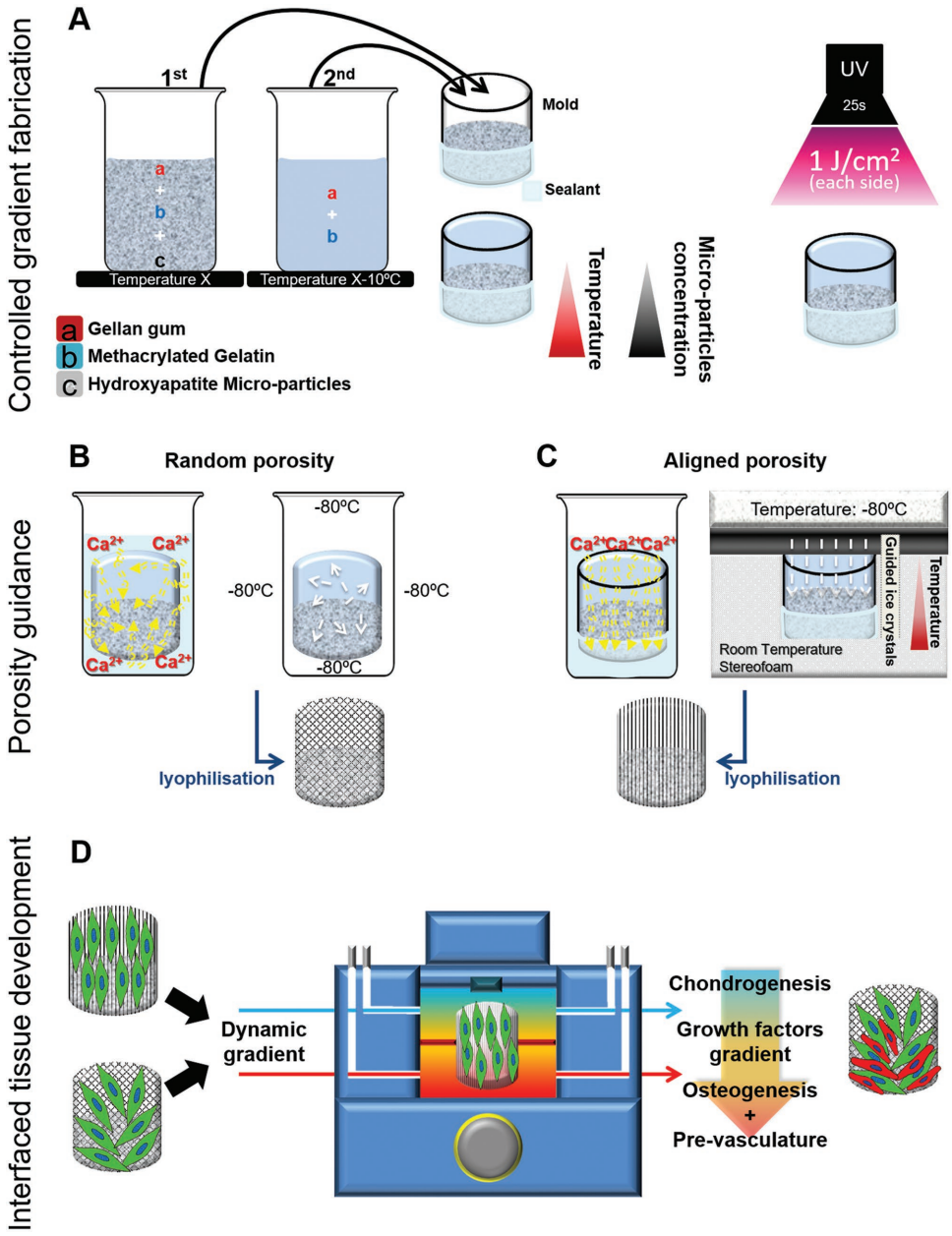

Figure 1. Schematic representation of 3D gradient and porosity guided structure fabrication. A) Gradient production combining three polymer/microparticle phases: a) ionically crosslinked polymer—gellan gum (gg), b) photo-crosslinked polymer—methacrylated gelatin (GelMA)—and concentration gradient represented by c) microparticle dispersion—hydroxyapatite microparticles (HAp). The control over temperature was considered for the mix in the interface of both polymeric phases, being the second solution added at a lower temperature in comparison with the first one, in order to control the convection of the aqueous mix. Obtained gels were first photo-crosslinked by UV exposure for a primary covalent crosslinking. Second, ionic crosslinking was performed by immersing the gel in a Ca^{2+} solution B) without the silicon mold or C) guided by isolating the gel in a silicon mold with open top surface. After crosslinking, the freezing step was also controlled to avoid losing the directional crosslinking of the polymeric chains promoted in the previous step. Keeping the silicon mold and adding an external cover of styrofoam around the mold, a temperature gradient was created to force linear ice crystals grow. D) A bioreactor device was designed to culture cells in 3D anisotropic and isotropic gradient constructs, combining the HAp gradient with growth factor cues from culture media.

To study the ability of inducing cell orientation guidance, using the developed dual-chamber bioreactor (Figure 4A-ii), fat-pad ASCs were cultured in anisotropic and isotropic scaffolds and evaluated in the three different regions of the 3D constructs, chondrogenic, interface, and osteogenic (Figure 4A-iii).

The cell directional distribution induced by the pore orientation was assessed in the anisotropic and isotropic structures (Figure 4B). At 21 d, chondrogenic, interfacial and osteogenic regions were quantified, respectively (Figure 4C). Interestingly, specific cell arrangements were dependent on each condition.

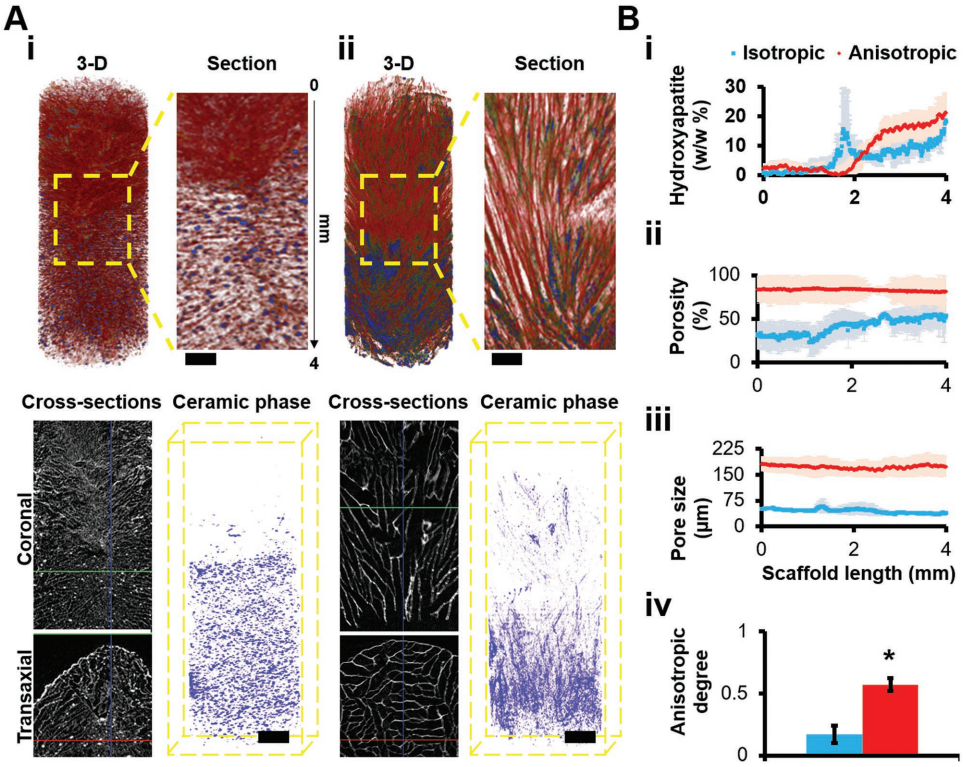

Figure 2. Structural characterization of 3D gradient structures. A) X-ray computed microtomographic (micro-CT) 3D reconstruction of i) random and ii) linear porous—isotropic and anisotropic—structures. Red color represents methacrylated gelatin (GelMA)-methacrylated gellan gum (MAGG) blended polymers, blue color represents the HAp (Section's scale bar = 0.5 mm). Coronal and transaxial sections of the bilayered phased structures are represented, showing its continuous interface. The ceramic phase distribution is represented inside the structure's volume. Scale bar = 1 mm. B) Profiles of: i) HAp distribution, ii) porosity percentage, iii) mean pore size, were traced for each condition for linear and random pore orientation (standard deviation represented by shaded colors), and iv) the anisotropic degree was assessed for each porous architecture, showing the higher anisotropic shape of the linear porous—anisotropic—structures. Values of anisotropic degree range from 0 (isotropic) to 1 (anisotropic). Data expressed as (mean ± standard error (SE)). *P*-value = 0.05, $N = 3$.

Cells cultured in the anisotropic structure were organized in a specific orientation at a higher frequency, as evidenced by the distribution peaks formed (Figure 4C-i), which were absent in the isotropic condition (Figure 4C-ii), correlated to a random organization. Further, the cell shape clearly varied per region, depending on the differentiation process happening in different regions of a single construct.

To quantify the cell distribution in each half of the 3D construct, fat pad-ASCs were cultured for 3 d before adding differentiation media. The metabolic activity assessment demonstrated a similar quantification in both halves (**Figure 5**A-i), representing a homogeneous cell distribution in the gradient structure.

To evaluate the commitment of cells toward the chondrogenic and osteogenic lineages, the expression of chondrogenic and osteogenic markers, e.g., RUNX2, osteocalcin (OCN) and osteopontin (OPN), and SOX9, were studied. Three regions were sliced: top, interface and bottom, to evaluate the impact of the biochemical gradient over stem cell codifferentiation (Figure 5A-ii). SOX9 chondrogenic marker significantly increased in the region with reduced or absent HAp concentration, named the chondrogenic region (top part, marked in blue). Osteogenic markers OCN, OPN, and RUXN2 were highly expressed in the HAp concentrated region, named the osteogenic region (bottom part, marked in red, Figures 4A-iii and 5B). Cells in the interface region presented significantly higher expression of SOX9 (2.4-fold increase, $p < 0.05$) compared to the osteogenic, but lower (4.1-fold decrease) in comparison with the chondrogenic one. Further, significantly lower expression of OCN (2.1-fold), RUNX2 (5.5-fold), and OPN (4.3-fold) was observed in the interface when compared to the osteogenic region ($p < 0.05$). Also, isotropic porous organization significantly increased the expression of the chondrogenic marker SOX9 (1.5-fold) and the osteogenic marker OCN (2.6-fold) on the chondrogenic region of the construct when compared to the anisotropic ones ($p < 0.05$, Figure 5B-i,ii,C-iii).

Finally, to assess the effect of a biochemical change on the prevasculature formation over a short period of time in the gradient structures, human adipose-derived microvascular endothelial cells (hAMECs) with fat pad-ASCs (Figure 5C-i) were cocultured with a basal condition over 5 d, and then perfused with two different media cocktails—basal and osteogenic (proangiogenic) conditions, until day 7. Strikingly, this biochemical change at day 5 demonstrated a spatial-temporal control over prevasculature, inducing its formation (Figure 5C-ii). Moreover, cell adhesion, shape, and distribution of prestained hAMECs (Figure 5D), demonstrated a cell morphology change from day 5 to 7 (Figure 5D-i–iv). The endothelial cells were dispersed and rounded in the basal condition (Figure 5D-iii) and were arranged in an elongated shape creating networks

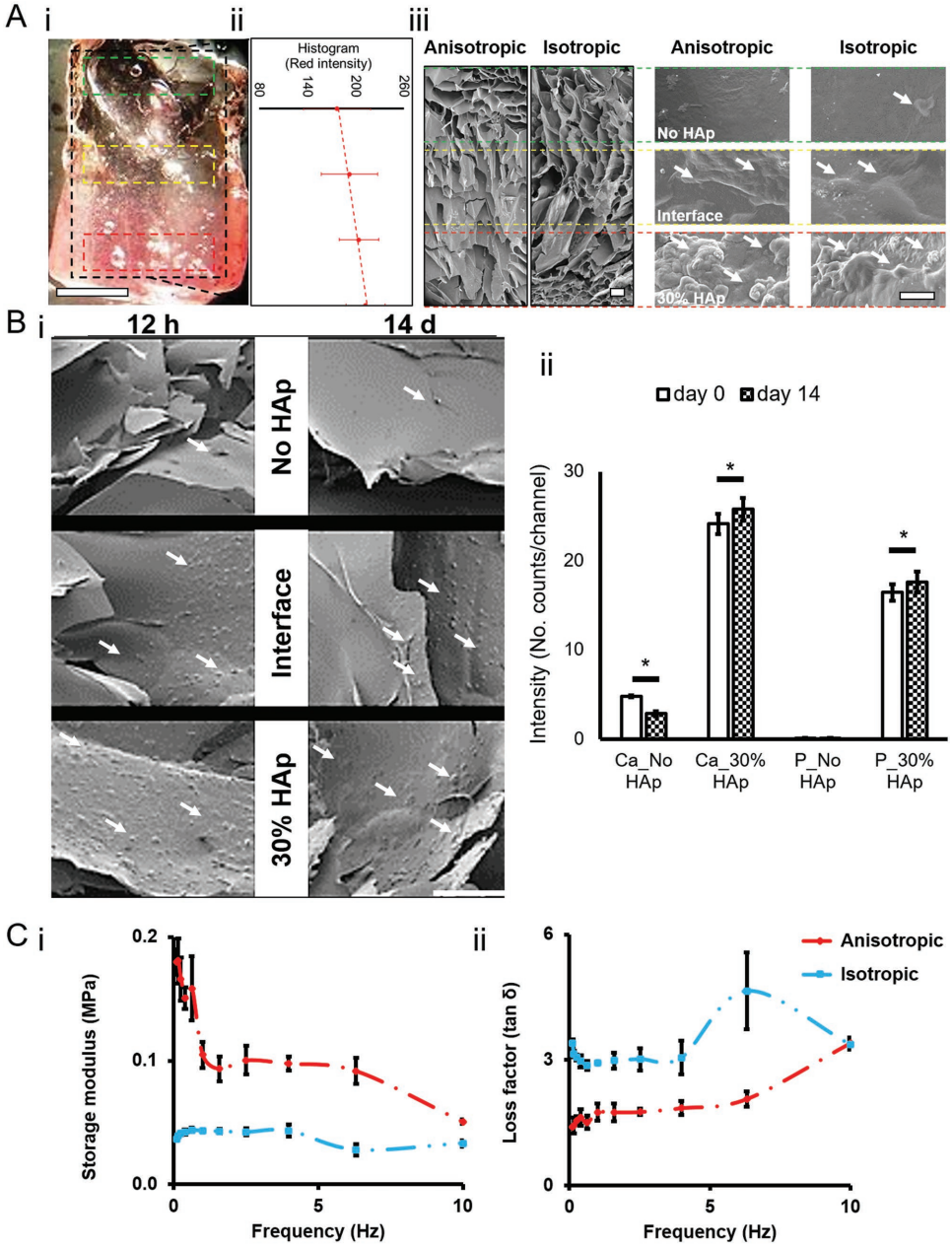

Figure 3. Physicochemical characterization of gradient structures. A) Image of the gradient structure after freeze-drying process and i) staining with alizarin red to show the HAp distribution profile (scale bar = 2 mm). ii) Red channel quantification from red-green-blue (RGB) histograms ($n = 4$). iii) SEM images at 13 × (scale bar = 500 µm) and 1000 × magnification (scale bar = 10 µm) showed the pore shape and wall orientation of anisotropic and isotropic architectures, respectively, and the HAp incorporation in the polymeric structure along its gradient after freeze drying (white arrows indicate the HAp). B) The transition from residual to rich HAp regions is represented by i) SEM images (scale bar = 400 µm) showing the HAp, as indicated by the white arrows. ii) Calcium (Ca) and phosphorus (P) were quantified per region by energy-dispersive X-ray spectroscopy (EDS) at day 0 and 14 of incubation in simulated body fluid (SBF) at 37 °C. The apatite layer disappears from the HAp rich to the HAp residual region, as required for OC differentiation (osteogenesis and chondrogenesis, respectively). C) Dynamic mechanical analysis (DMA) was performed to the entire gradient structures. The stress was applied by forced set frequency to the samples to obtain deformation and a phase angle. These data allowed the calculation of i) storage modulus, and ii) the tan delta (δ). Data expressed as (mean ± SE), $n = 3$.

in the endo-osteogenic proangiogenic medium (Figure 5D-iv). The tubular-like segments were identified in both conditions (Figure 5D-v,vi) and quantified, showing a significant increase of ≈35% in the region cultured with the endo-osteogenic cocktail condition (Figure 5D-vii).

3. Discussion

A simple, versatile, and controllable methodology was developed to produce 3D isotropic and anisotropic GelMA-low acyl Gellan-gum (LAGG) scaffold with HAp gradients. The use of

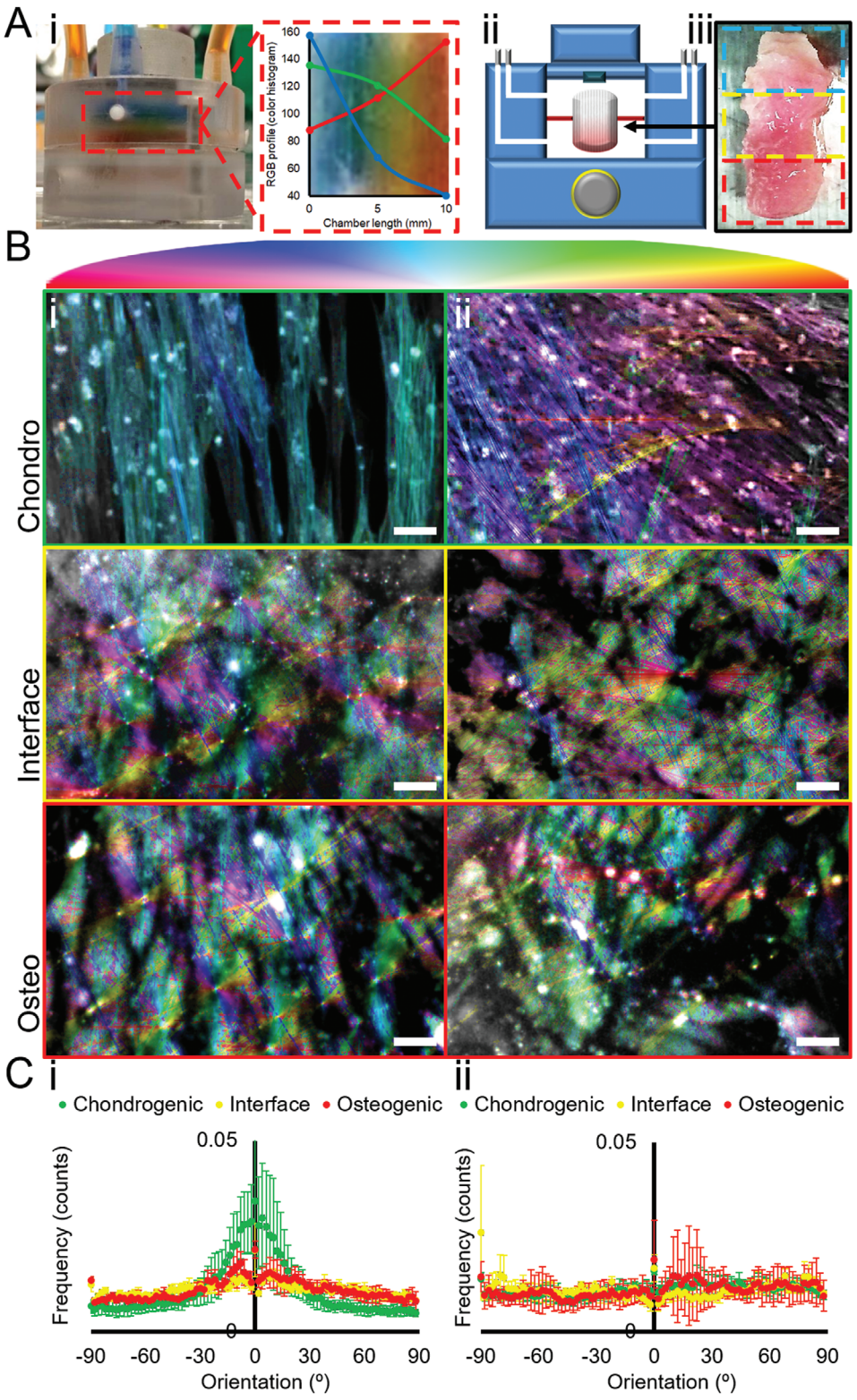

Figure 4. Cell orientation assessment in 3D gradient structures. A) The bioreactor device, designed for generating chemical gradients, was perfused with i) two dyes (red and blue), creating a yellow interface. The color profile was traced showing the gradient formed in an RGB histogram. ii) Thus, the bioreactor was designed to comprise two compartments in a dual-chamber, interfaced by a 3D construct. iii) The constructs were cultured for osteo- and chondrogenesis in the custom designed dual-chambers to coordinate the structure gradient along with the biochemical gradient (scale bar = 1 mm). B) Cells were cultured in the dual-chamber bioreactor device. Fat pad ASCs were seeded in i) anisotropic and ii) isotropic structures and the resulting constructs were cultured for 21 d. Microscopic images were treated using ImageJ[33] (National Institutes of Health (NIH), v. 1.52e, http://imagej.nih.gov/ij)

two different polymers, GelMA and LAGG, blended in two solutions, at controlled temperatures, allowed the use of convective forces to drive the dispersion of microparticles in the 3D space, which creates HAp gradients. Photo-crosslinking was applied to form a hydrogel and maintain the gradient. The formation of gradients by thermal changes in fluidic interfaces was previously demonstrated,[35] but has not been applied to biological systems. In the present study, the fabricated gradient of HAp distribution resembles the transition of apatite layer that characterizes the OC interface of human articular joints.[36]

After achieving the controlled formation of HAp concentration gradients in GelMA-LAGG gels, linear and random porosities typical of anisotropic and isotropic structures, respectively, was generated by crosslinking and freeze-drying mechanisms. Guided ionic crosslinking was performed by vertically diffusing a calcium solution into the gels, resulting in a vertical arrangement of the hydrogel's LAGG molecular chains. This approach was previously tested[37] and theoretically described[38] for alginate solutions, but not applied for other polymers, such as LAGG. Then, this approach was combined with directional freezing to obtain anisotropic scaffolds with a gradient distribution of microparticles. A range of temperatures from −80 °C to room temperature (RT) promoted an aligned ice crystal growth in the direction of the higher temperature during the freezing process. The anisotropic configuration was fabricated after freeze drying without losing the HAp gradient while the isotropic porous architecture induced the formation of two peaks at the two end of HAp layer, including the transition region between the first and second layer. This may due to repelling force of ice formation during the isotropic freezing. In anisotropic freezing, the temperature ramp neutralized the repelling force of ice nucleation, contributing to make it progressively increasing, as it is important for OC interface. In respect to these HAp gradient differences, the formation of anisotropic porosity contributed to improve the interface integration, as shown by the absence of the HAp peak, and decreased the HAp dispersion, as represented by the smaller standard deviation (Figure 2B-i). The isotropic condition increased the randomization of the HAp gradient distribution and the formed peak of HAp is correlated with the formation of a sharper interface since the polymeric walls grow in every direction, and not only vertically, under this condition. Thus, the anisotropic condition positively contributed to the generation of a smoother interface. Overall, in the present study, we for the first time combined two principles previously and independently described: guided crosslinking[37] and freezing[39] mechanisms to create anisotropy in hydrogels presenting microparticle gradients formed by convection in creaming emulsions.[40] The combination of such principles in hydrogels made of LAGG-GelMA polymeric blends allowed to combine a polysaccharide with a fibrous protein, as it is representative of the native ECM, generating patterned gradients of HAp with controlled porosity orientation.

The fabricated isotropic and anisotropic gradient structures showed, at the same polymeric concentration, not only differences in storage modulus but also in cell adhesion and proliferation (Figures S7 and S8, Supporting Information). Further, GelMA and LAGG presented different degradation rates. Thus, by tuning the polymeric blend, several features of the anisotropic structures can be adjusted and create simultaneous control over degradation rate and elasticity to be applied in biological systems.

The development of physiologically relevant models requires an understanding of the tissue architecture and physiology. The OC interface is composed of two main tissues, cartilage and bone, which differ substantially.[30] Although bone and cartilage are heterogeneous tissues as many other interfaces in nature, they were proven to be generated from one continuous developmental lineage.[41] Thus, using a single stem cell type to create a tissue interface required a spatial control over the 3D environment, which was achieved by the custom-made bioreactor previously designed in-house for biochemical gradients.[42,43] ASCs isolated from human fat pad removed during arthroscopic surgical interventions. These cells were used to perform the codifferentiation assays, since this fat pad is located in the infrapatellar knee joint, the target tissue of the developed strategy. The dual-chamber bioreactor allowed to control the mixing of two different culture media creating a three-layered environment. Osteogenic, chondrogenic, and their mixed culture medium cocktail at the interface induced phenotypic changes observed in the ASCs through different regions of a single construct. As demonstrated by the marker expression, the codifferentiation of stem cells in a single environment was spatially controlled, which can potentially be applied for broader tissue interfaces.

Currently, there is increasing evidence from in vivo and clinical studies that subchondral bone lesions may precede cartilage degeneration.[44] So, osteoarthritis is considered an OC disease and possibly bone dependent because of the inflammatory factors delivered by the vasculature present in the subchondral bone.[45] Blood vessels from the subchondral bone invade the articular cartilage promoting the progression of osteoarthritis and forming osteophytes.[46] However, hyaline healthy cartilage is avascular while subchondral bone is vascular. To target this spatial control over prevasculature formation, ASCs from fat pad were cocultured with hAMECs. Importantly, this approach aimed at providing solutions not only to mimic the lesion condition in vitro but also to improve osteogenesis. ECs secrete factors such as fibroblast growth factors, interleukin (IL)-1, and IL-6, and nitric oxide that influence osteoclast behavior, thereby regulating bone formation and resorption as previously shown.[47,48] In turn, synergistically ECs are the target of many bone-derived signals, such as parathyroid hormone, insulin-like growth factors types 1 and 2, basic fibroblast growth factor, platelet-derived growth factor, and vascular endothelial growth factor (VEGF).[49,50] Although these events are well studied and reported for 2D in vitro conditions, 3D structure still requires a better understanding and control. Using a gradient of culture media from osteogenic to basal conditions, the coculture promoted the formation of a prevasculature in the region perfused by the osteogenic-endothelial media

to assess cell orientation (scale bar = 50 μm). A color map was also generated through ImageJ[33] according to cell orientation. C) Cell orientation was quantified per condition in i) anisotropic and ii) isotropic constructs. The presence of a peak means that the frequency of alignment is superior in a specific angle. Data expressed as (mean ± SE). $N = 5$.

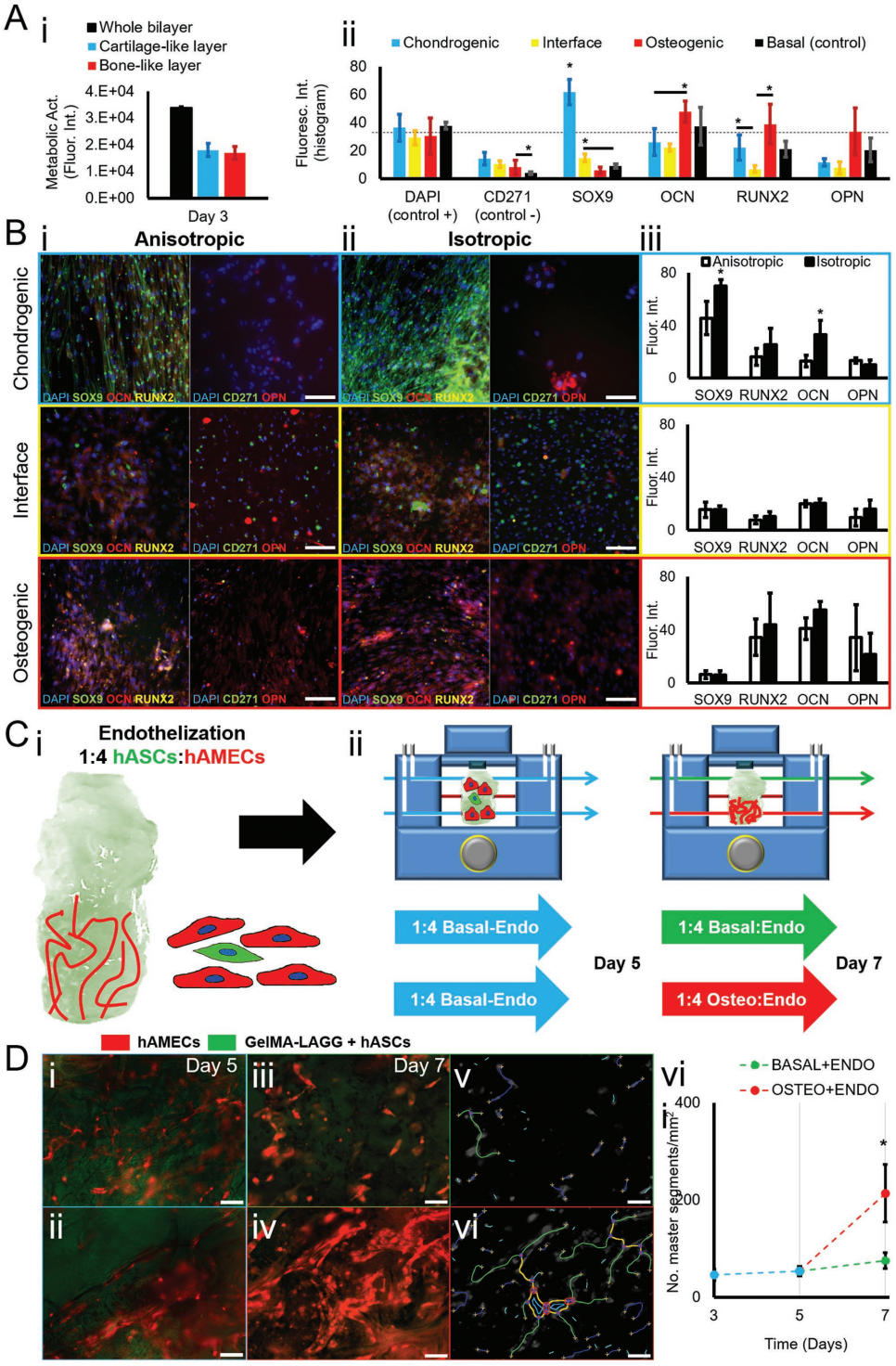

Figure 5. Structural and biochemical gradients for OC differentiation in isotropic and anisotropic 3D structures and prevasculature formation. A) Fat pad-ASCs were cultured in the gradient structures. i) Each layer was quantified for metabolic activity three days after seeding to assess the cell distribution through the whole scaffold. ii) Immunostaining was performed and quantified by fluorescent intensity to measure the expression of osteogenic and chondrogenic markers. RUNX2, osteocalcin (OCN), and osteopontin (OPN) were selected as osteogenic-related markers and SOX9 as a chondrogenic-related marker. The quantification of these markers was evaluated against a nondifferentiated control of hASCs cultured in basal medium. B) hASCs were seeded into i) anisotropic and ii) isotropic structures and differentiated over 21 d (scale bar = 100 µm). iii) Immunostaining of RUNX2, OCN, OPN, and SOX9 markers was performed and quantified to assess cell organization and marker expression in both architectures. C) hASCs isolated from fat pad were cocultured with hAMECs over 7 d. i) The seeding was performed onto the structures in a ratio of 1:4 (scale bar = 1 mm). ii) Two interfaced culture media were perfused into the dual-chamber: The mixture was prepared as 4:1 endo-basal or endo-osteogenic, accordingly to the maintenance or differentiation conditions, and perfused after keeping the whole construct for 5 d in basal culture medium. D) hAMECs were

cocktail. This can potentially be explained by the differentiation of ASCs toward osteogenesis, which possibly induces the secretion of VEGF, stimulating the formation of endothelial vascular networks.

Moreover, the creation of a gradient with control over porosity is of major importance with possible applications in materials engineering and regenerative medicine, such as tissue in vitro modeling and drug discovery. The materials engineered approaches together with the automated cell devices can potentiate the acceptance and integration of such strategies in more robust and reproducible industrial approaches.

In conclusion, the developed strategy allowed the fabrication of microparticle gradients which were not destroyed when controlled simultaneously with the porosity orientation. Further, the quantitative correlation between the pore orientations and the mechanical properties was investigated revealing an increase in storage modulus in anisotropic structures, while loss modulus was increased in the isotropic ones. Thus, a user-friendly and reproducible method to fabricate 3D gradient structures of bioactive signals in isotropic or anisotropic porous architectures was established. Moreover, we demonstrated the spatial control over OC markers as it is relevant for interfaced 3D tissues. Importantly, prevasculature formation was upregulated in the bone-like region while it was downregulated in the cartilage-like region of the same construct. Overall, the presented fabrication technique and biological results demonstrated, have a direct impact on the tissue engineering field for fabrication of hierarchically organized tissues, such as the OC unit, with broader potential applications for fabrication of tissue mimics, regenerative medicine and drug screening and discovery using 3D in vitro tissue modeling.

4. Experimental Section

Materials: LAGG (Gelzan CM, $F = 1\ 000\ 000$), gelatin (from porcine skin, gel strength 300, Type A), and methacrylic anhydride were obtained from Sigma-Aldrich (USA). Unless otherwise stated all the reagents were purchased from Sigma-Aldrich.

Hydroxyapatite Microparticles Synthesis (HAp): HAp was produced by precipitation reaction of calcium hydroxide (Riedel-de Haën, Germany) and orthophosphoric acid 85% (Panreac, Spain) solutions in an aqueous system at RT. The mixing was gently performed at pH 11, adjusted by addition of concentrated ammonium hydroxide (1 M, Riedel-de Haën, Germany), with a continuous flow rate ranging from 8 to 15 mL min^{-1}. The formed ceramic powder was sieved to obtain particles smaller than 250 µm.

X-ray Bragg–Brentano diffractometer (Bruker D8 Advance DaVinci, Germany) employing Cu-K_α radiation ($\lambda = 0.154056$ nm) at 40 kV and 40 mA was used to analyze the crystallinity of the HAp. Data were collected from 10° to 70° (2θ values), with a step size of 0.04°, and a counting time of 2 s per step.

Methacrylation of Gelatin (GelMA): Gelatin was modified by methacrylation. A solution of gelatin (from porcine skin, Type A, 300 mw, Sigma) at 10% (w/v) was prepared by dissolving 2 g in 20 mL of phosphate-buffered saline (PBS), at 50 °C for 1 h and covered to avoid evaporation. 0.8 mL per gram of gelatin of methacrylic anhydride were added to the solution at a rate of 0.1 mL min^{-1}, counting 16 min down. The beaker was covered with aluminum to avoid light, and the temperature was kept between 42 and 48 °C during the addition. Methacrylic anhydride was directly added to gelatin solution under stirring of ≈160 rpm. The solution was left to react for 2 h while temperature was kept between 40 and 45 °C at a slow stirring of ≈120 rpm.

To finalize the reaction, the solution was added to a prewarmed dialysis bag (12–14 kDA cutoff) without precipitation of the solute. Dialysis was performed against distilled water in a 5 L beaker for one week keeping the temperature around 45 °C to avoid gelation. Distilled water was changed three times at the preparation day and once a day afterward.

After 1 week, GelMA solution was removed from dialysis membrane and transferred to 50 mL falcon tube. The solution was frozen in liquid nitrogen or at –80 °C (this second options requires waiting for 1 d of freezing before drying). Freeze drying was performed in a freeze drier for 5 d. Lyophilized GelMA was frozen at –80 °C until further use.

2,4,6-trinitrobenzene sulfonic acid (TNBSA) was used to determine the free amino groups in GelMA to determine the modification degree. Absorbance and concentration present a linear relationship up to 1 mg mL^{-1}. The modification of gelatin by methacrylation is inversely proportionally to the absorbance of the solutions at 335 nm. The determination of the concentration of primary amines was correlated to the substitution of these amines by methacrylation. The extinction coefficient was used to calculate the total percentage of modification by comparison to amino acid standards as a calibration.

Preparation of GelMA and LAGG 3D Gradient Structures: LAGG and GelMA were dissolved at a total polymer concentration of 2% (w/v) in two separated beakers. First, LAGG was dissolved at 80 °C for 1 h in distilled water. Then, the solution was cooled down to 50 °C, and 0.5% (w/v) 2-hydroxy-1-[4-(2-hydroxyethoxy)phenyl]-2-methyl-1-propanone (Irgacure 2959, Ciba Specialty Chemicals) was added to the polymeric solution and dissolved for 1 h. GelMA was then added for dissolution for 1 h at 45 °C. HAp was added at 30% (w/w) and dispersed under stirring in one of the two beakers with the LAGG/GelMA solution. After complete HAp dispersion, 800 µL of this solution was added into a mold of 10 × 7 mm at 55 °C. A second injection of 800 µL was added on top of the first half at 45 °C within 30 s after pipetting the first gel. Afterward, hydrogels were obtained by immersing the gradients in α-minimum essential medium (MEM) medium without fetal bovine serum (FBS) for 24 h for total ionic-crosslinking of LAGG molecular chains. For the isotropic structure fabrication, the silicon molds were removed after 1 h in medium solution. For the fabrication of anisotropic structures, a guided ionic crosslinking was performed. To guide the ionic crosslinking, cylindrical molds were covered on the bottom part with Parafilm and immersed in culture medium solution. After 24 h at 37 °C, the ionic-crosslinked hydrogels were exposed to UV light (320–500 nm, 7.14 mW cm^{-2}, EXFO OmniCure S2000) for 60 s each side of the mold. After photo-crosslinking, a gradient temperature, reaching the –80 °C, was applied using metallic plates previously frozen in dry ice. To create the temperature gradient, a custom made styrofoam mold involving the silicone mold was used covering the polymeric solution all around except the top, where the frozen plate at –80 °C was directly placed for 2 h. After freeze drying, the fabricated structures were punched and sliced in cylinders of 4 mm × 3 mm. The structures were submitted to three cycles of oxygen plasma treatment, 5 min each, for sterilization and surface hydrophilicity cure before cell seeding.[51]

stained red with a live staining allowing continuous tracking. Scaffold and hASCs are represented as green (bright field) in the microscopic images (scale bar = 100 µm). Representative images for: i) top and ii) bottom regions were acquired. At day 5, iii) basal condition kept being perfused on the top region and iv) the osteogenic mix perfused on the bottom region. The v) top and vi) bottom regions of the scaffolds were analyzed to identify the tubular segments created per region. vii) The tubular segments were identified in the microscopic images using Angiogenesis Analyzer[34] tool for ImageJ[33] (NIH, v. 1.52e, http://imagej.nih.gov/ij). These segments were quantified per area and their formation profile was traced at three time-points, 3, 5, and 7 d. Data expressed as (mean ± SE). $N = 5$, P-value = 0.05.

DMA: The viscoelastic measurements were performed using a TRITEC8000B dynamic mechanical analyzer (Triton Technology, UK) in the compressive mode. The measurements were carried out at 37 °C. Samples were cut into cylindrical shapes of ≈8 mm diameter and 6 mm thickness (measured each sample accurately with a micrometer). The scaffolds were always analyzed whilst immersed in a liquid bath placed in a Teflon reservoir. The scaffolds had previously been immersed in phosphate buffer solution (PBS) until equilibrium was reached (37 °C overnight). The geometry of the samples was then measured and the samples were clamped in the DMA apparatus. After equilibration at 37 °C, the DMA spectra were obtained during a frequency scan between 0.1 and 10 Hz. The experiments were performed under a constant strain amplitude (50 µm). A small preload was applied to each sample to ensure that the entire scaffold surface was in contact with the compression plates before testing, and the distance between plates was equal for all scaffolds being tested. A minimum of three samples were used for each condition.

Scanning Electron Microscopy Analysis: The 3D gradient structures were analyzed by EDS (SEM/EDS, NanoSEM-FEI Nova 200, USA) to assess the bioactivity of the structures shown by apatite formation. Prior the microstructure imaging by SEM, specimens were coated with gold using a Fisons Instruments Coater (Quorum/Polaron E6700, UK) at 18 mA for 120 s. SEM was performed to evaluate structure wall thickness and surface morphology.

FTIR Analysis: Infrared spectra of the HAp were obtained by Fourier transform infrared spectrometry (FTIR model IRPrestige 21, Shimadzu, USA). For this purpose, HAp were mixed with KBr in the proportion of 1/150 (by weight) and pressed into a pellet. To assess the amorphous state of HAp in the structures, FTIR-attenuated total reflection (ATR) was performed instead. Each infrared spectrum was on the average between 32 and 40 scans over a range of 800–4400 cm^{-1} collected with a resolution of 4 cm^{-1} at room temperature.

X-Ray Diffraction Analysis: The qualitative and quantitative analyses of crystalline phases presented on the powders and scaffolds were obtained by XRD using a conventional Bragg–Brentano diffractometer (Bruker D8 Advance DaVinci, Germany) equipped with CuK_α radiation, produced at 40 kV and 40 mA. Data sets were collected in the 2θ range of 10°–70° with a step size of 0.04° and 2 s for each step. The phase composition of the powders was calculated on the basis of XRD patterns by means of Rietveld analysis with TOPAS 5.0 software (Bruker, Germany). Refined parameters were scale factor, sample displacement, background as Chebyshev polynomial of fifth order, crystallite size, and lattice parameters.

Assessment of Degradation Rate: GelMA and LAGG polymeric scaffolds were assessed for degradation over 14 and 30 d, respectively. Weighed hydrogels ($n = 6$) were incubated in a 24 ng mL^{-1} collagenase type I solution at 37 °C. The samples were removed, the excess of water adsorbed, and then freeze dried and weighed again to determine weight loss.

$$\text{Weightloss}(\%) = \frac{(m_0 - m_f)}{m_0} \times 100\% \quad (1)$$

where m is mass, 0 is initial, and f is final.

3D Architecture Characterization of 3D Porous Structures and HAp Profile: Freeze-dried structures were analyzed by micro-CT. The gradient structures were acquired by X-ray diffraction and then reconstructed for qualitative and quantitative analyses. HAp profile, porosity, mean pores size, and anisotropic degree were quantified. 3D cross-sections of isotropic and anisotropic structures were designed. Samples were acquired with a SkyScan 1272 scanner (v1.1.3, Bruker, Boston, USA), with a pixel size of 10 µm. Approximately 300 projections were acquired over a rotation range of 180°, with a rotation step of 0.6°. Data sets were reconstructed using standardized cone-beam reconstruction software (NRecon 1.6.10.2, Bruker). The output format for each sample was bitmap images. Representative data set of the slices was segmented into binary images with a dynamic threshold of 30–255 for soft polymer analysis and 120–2255 for ceramic phase analysis (gray scale values). Then, the binary images were used for morphometric analysis (CT Analyser, v1.13, Bruker) and to build the 3D models.

Alamar Blue Assay: NIH-3T3 fibroblasts were seeded and cultured as previously described. After 3 h, the constructs were moved to new 24-well suspension culture plate and incubated with 900 µL of basal medium (α-MEM supplemented with 10% FBS, 1% A/A. The previously defined medium was used and changed at least twice weekly. Metabolic activity was evaluated after 1 and 7 d of culture with AlamarBlue CellTiter-Glo Luminescent Cell Viability Assay (Promega, Madison, WI, USA) ($n = 9$), according to the manufacturer's instructions. Briefly, the medium was removed, samples washed and incubated in 10% (v/v) AlamarBlue solution in basal medium, at 37 °C. The obtained supernatant was transferred to a 96-well plate and the fluorescence measured in a microplate reader. Then, the medium was removed by aspiration and the constructs were washed with fresh medium three times and kept in culture until the end of the assay. Scaffolds without cells were used as a negative control for fluorescent intensity correction.

Isolation and Culture of Fat Pad ASCs: ASCs were isolated from human tissues obtained from Hoffa's body removal during arthroscopic surgeries on male and female donors with ages between 19 and 32 years, after informed consent, under cooperation protocols established with Centro Hospitalar Póvoa do Varzim and Clínica Saúde-Atlântica. The study has been approved by the Ethical Committee of Centro Hospitalar Póvoa do Varzim, Grupo Saúde-Atlântica and University of Minho. All experiments were carried out according to animal care standards set forth by the National Institute of Health and were approved by the Institutional Animal Care and Use Committee (IACUC) at Stanford University.

All the samples were processed within 24 h after the arthroscopic procedure to the knee and human hASCs were enzymatically isolated from Hoffa's body. hASCs were isolated following an enzymatic digestion-based method with type II collagenase (Sigma) from Hoffa's body human tissue. The extracted tissue was placed in PBS solution and washed several times with 1% PBS/AA (v/v) solution, until blood or other bodily contaminants were totally removed, and cut into small pieces. Tissue digestion was performed by incubating, at 37 °C in a humidified atmosphere of 5% CO_2 for 1–2 h, the small pieces with 10–20 mL of a mixture composed by cell medium MEM alpha medium (Gibco), supplemented with 10% FBS and 1% A/A mixture, and type II collagenase (1:1). The digested tissue was filtered and cell suspension centrifuged at 1220 rpm for 5 min. The isolated cell populations were expanded in MEM alpha medium supplemented with 10% FBS and 1% of A/A mixture until reaching confluence.

Fat pad ASCs were cultured in bilayered structures for 3 d, before starting cell differentiation. The cells were seeded in a concentration of 1×10^6 cells per scaffold, having these scaffolds 6 mm × 4 mm high and diameter, respectively. At day 3, the two layers of each structure were divided and measured the metabolic activity of each layer versus the whole scaffold, in order to assess cell distribution in each layer.

hASCs were cultured for 21 d in osteogenic differentiation medium. For osteogenic induction medium, MEM alpha was supplemented with dexamethasone (100×10^{-9} M), β-glicerophosphate (10×10^{-3} M), ascorbic acid 2-phosphate (50 mg mL^{-1}), 1% AB, and 10% FBS. Chondrogenic medium was prepared supplementing Dulbecco's modified Eagle's medium high-glucose with dexamethasone (100×10^{-9} M), ascorbic acid 2-phosphate (50 µg mL^{-1}), L-proline (40 µg mL^{-1}), transforming growth factor-β3 (10 ng mL^{-1}), 1% AB, and 10% FBS.

Coculture of Fat Pad ASCs with Human Adipose Microvascular Endothelial Cells (hAMECs) Using a Dual-Chamber Bioreactor: hAMECs were stained with DiI live staining (Thermo Fischer Scientific) and then mixed with ASCs in a ratio of 4:1, respectively. The mixed population was seeded in the top and bottom parts of the isotropic porous 3D structures placed in the dual-chamber bioreactor. Basal MEM alpha supplemented with 10% FBS and 1% A/A was mixed with endothelium growth medium (Lonza) containing 2% FBS and VEGF in a ratio of 1:4, respectively, and equally perfused in both compartments of the dual-chamber. The bioreactor chamber was perfused at 5 µL min^{-1} and placed at 37 °C in a humidified 5% CO_2 atmosphere. After 5 d of perfusion, the cell culture medium in the bottom chamber was changed by the mix of osteogenic differentiation medium (Lonza) with endothelial growth medium (1:4). Constructs were perfused for further 2 d more.

Construct were imaged on top and bottom regions at day 5 and 7 by fluorescent microscopy. ImageJ[33]/FIJI[52] (NIH, v. 1.52e, http://imagej.nih.gov/ij) plugin Angiogenesis Analyzer[34] was applied to evaluate the major segments formation. Bright field and fluorescent images were individually analyzed and their outcomes were combined in average to reduce potential artefacts occurring in each image type ($n = 5$).

Immunofluorescence Staining: Cells in constructs were fixed with 4% paraformaldehyde for 20 min at RT. Fixed cells were washed with PBS, nonspecific binding was blocked with 1% bovine serum albumin (BSA) (Sigma) and permeabilized with 0.3% Triton-X 100 (Sigma) for 2 h at RT. Cells were incubated with rabbit anti-osteocalcin (Millipore), mouse anti-SOX9 (Santa Cruz Biotechnology), and goat anti-RUNX2 (Novus Biologicals) overnight at 4 °C. Afterward, samples were washed and incubated with secondary goat anti-mouse Alexa Fluor 568, Alexa Fluor 647, and goat anti-mouse Alexa Fluor 488 antibodies (Life Technologies) for 2 h at RT. Mouse anti-osteopontin (Abcam) was visualized with using the secondary antibody Alexa Fluor 568 (Life Technologies). CD271-APC (BioLegend) was used as a negative control staining. Finally, cell nuclei were counterstained with 4,6-diamidino-2-phenyindole dilactate (Invitrogen). All samples were visualized by fluorescence microscopy (Zeiss LSM710 inverted confocal microscope). Fluorescent quantifications were carried out through ImageJ[33]/FIJI[52] (NIH, v. 1.52e, http://imagej.nih.gov/ij).

Statistical Analysis: All results expressed as mean ± standard deviation or confidence interval. Student's *t*-test was used to compare group means, and a *p*-level <0.05 was considered statistically significant. Statistical analyses were performed with Microsoft Excel 2010 and GraphPad Prism 5 software for Windows. Not-paired two-tailed Student's *t*-test and nonparametric Mann–Whitney test were used.

Supporting Information

Supporting Information is available from the Wiley Online Library or from the author.

Acknowledgements

The authors are grateful for the Fundação para a Ciência e a Tecnologia (FCT) distinctions attributed to R. F. Canadas (SFRH/BD/92565/2013), who was awarded a PhD scholarship and to J.M.O. (IF/00423/2012 and IF/01285/2015). The authors acknowledge that this material and collaboration is based in part upon work supported by Luso-American Development Foundation (FLAD). This work was supported in part by the European Research Council Grant agreement ERC-2012-ADG 20120216-321266 for project ComplexiTE. The authors would like to acknowledge the National Science Foundation under Award No. NSF 1547791 and by the Office of the Assistant Secretary of Defense for Health Affairs under Award No. W81XWH-15-1-0576. Opinions, interpretations, conclusions, and recommendations are those of the author and are not necessarily endorsed by the National Institutes of Health or the Department of Defense. The authors also thank SAR—Soluções de Automação e Robótica for the support with bioreactor development, to João Costa (3B's Research Group) for the assistance with dynamic mechanical analysis, to I. F. Cengiz (3B's Research Group) and Filipe Carvalho (3B's Research Group) for their help with material shipment and micro-CT analysis, and to Alessandro Tocchio (BAMM Lab) for their helpful and inspiring discussions.

Conflict of Interest

The authors declare no conflict of interest.

Keywords

anisotropy, biochemical gradients, heterotypic tissues, microparticle gradients

Received: June 15, 2018
Revised: September 10, 2018
Published online:

[1] X. Wu, P. Jiang, L. Chen, F. Yuan, Y. T. Zhu, *Proc. Natl. Acad. Sci. USA* **2014**, *111*, 7197.
[2] J. B. Gurdon, P.-Y. Bourillot, *Nature* **2001**, *413*, 797.
[3] J. E. Samorezov, E. Alsberg, *Adv. Drug Delivery Rev.* **2015**, *84*, 45.
[4] U. Ahmed, A. Anwar, R. S. Savage, M. L. Costa, N. Mackay, A. Filer, K. Raza, R. A. Watts, P. G. Winyard, J. Tarr, R. C. Haigh, P. J. Thornalley, N. Rabbani, *Sci. Rep.* **2015**, *5*, 9259.
[5] M. Singh, C. Berkland, M. S. Detamore, *Tissue Eng., Part B* **2008**, *14*, 341.
[6] H. H. Lu, S. Thomopoulos, *Annu. Rev. Biomed. Eng.* **2013**, *15*, 201.
[7] U. A. Gurkan, R. El Assal, S. E. Yildiz, Y. Sung, A. J. Trachtenberg, W. P. Kuo, U. Demirci, *Mol. Pharmaceutics* **2014**, *11*, 2151.
[8] M. Lei, L. J. Schumacher, Y.-C. Lai, W.-T. Juan, C.-Y. Yeh, P. Wu, T.-X. Jiang, R. E. Baker, R. B. Widelitz, L. Yang, C.-M. Chuong, *Proc. Natl. Acad. Sci. USA* **2017**, *114*, E7101.
[9] D. Buxhoeveden, W. Lefkowitz, P. Loats, E. Armstrong, *Anat. Embryol.* **1996**, *194*, 23.
[10] S. N. Sansom, F. J. Livesey, *Cold Spring Harbor Perspect. Biol.* **2009**, *1*, a002519.
[11] W. J. Polacheck, A. E. German, A. Mammoto, D. E. Ingber, R. D. Kamm, *Proc. Natl. Acad. Sci. USA* **2014**, *111*, 2447.
[12] J. Cassidy, A. Hiltner, E. Baer, *Connect. Tissue Res.* **1989**, *23*, 75.
[13] C. Bonnans, J. Chou, Z. Werb, *Nat. Rev. Mol. Cell Biol.* **2014**, *15*, 786.
[14] N. H. Dormer, C. J. Berkland, M. S. Detamore, *Ann. Biomed. Eng.* **2010**, *38*, 2121.
[15] R. Xu, A. Boudreau, M. J. Bissell, *Cancer Metastasis Rev.* **2009**, *28*, 167.
[16] F. Xu, C.-A. M. Wu, V. Rengarajan, T. D. Finley, H. O. Keles, Y. Sung, B. Li, U. A. Gurkan, U. Demirci, *Adv. Mater.* **2011**, *23*, 4254.
[17] T. Ren, Z. Mao, J. Guo, C. Gao, *Langmuir* **2013**, *29*, 6386.
[18] S. Tasoglu, C. H. Yu, H. I. Gungordu, S. Guven, T. Vural, U. Demirci, *Nat. Commun.* **2014**, *5*, 4702.
[19] L. Han, Z. Mao, J. Wu, Y. Guo, T. Ren, C. Gao, *Biomaterials* **2013**, *34*, 975.
[20] J. Wu, Z. Mao, H. Tan, L. Han, T. Ren, C. Gao, *Interface Focus* **2012**, *2*, 337.
[21] T. Ren, S. Yu, Z. Mao, S. E. Moya, L. Han, C. Gao, *Biomacromolecules* **2014**, *15*, 2256.
[22] J. E. Phillips, K. L. Burns, J. M. Le Doux, R. E. Guldberg, A. J. García, *Proc. Natl. Acad. Sci. USA* **2008**, *105*, 12170.
[23] X. Feng, W. C. Max, R. Venkatakrishnan, F. T. Dylan, K. H. Onur, S. Yuree, L. Baoqiang, G. U. Atakan, U. Demirci, *Adv. Mater.* **2011**, *23*, 2454.
[24] T. S. Shim, S.-M. Yang, S.-H. Kim, *Nat. Commun.* **2015**, *6*, 6584.
[25] S. Tasoglu, E. Diller, S. Guven, M. Sitti, U. Demirci, *Nat. Commun.* **2014**, *5*, 3124.
[26] T. Alessandro, D. N. Gozde, S. Kaushik, M. Vigneshwaran, C. Bukre, E. A. Rami, D. Utkan, *Adv. Mater.* **2017**, *30*, 1705034.
[27] N. G. Durmus, H. C. Tekin, S. Guven, K. Sridhar, A. Arslan Yildiz, G. Calibasi, I. Ghiran, R. W. Davis, L. M. Steinmetz, U. Demirci, *Proc. Natl. Acad. Sci. USA* **2015**, *112*, E3661.
[28] S. G. M. Uzel, O. C. Amadi, T. M. Pearl, R. T. Lee, P. T. C. So, R. D. Kamm, *Small* **2016**, *12*, 612.
[29] A. Seidi, M. Ramalingam, I. Elloumi-Hannachi, S. Ostrovidov, A. Khademhosseini, *Acta Biomater.* **2011**, *7*, 1441.
[30] A. Di Luca, C. Van Blitterswijk, L. Moroni, *Birth Defects Res., Part C* **2015**, *105*, 34.

[31] S. Sant, M. J. Hancock, J. P. Donnelly, D. Iyer, A. Khademhosseini, *Can. J. Chem. Eng.* **2010**, *88*, 899.
[32] R. F. Canadas, T. Ren, A. Tocchio, A. P. Marques, J. M. Oliveira, R. L. Reis, U. Demirci, *Biomaterials* **2018**, *181*, 402.
[33] C. A. Schneider, W. S. Rasband, K. W. Eliceiri, *Nat. Methods* **2012**, *9*, 671.
[34] G. Carpentier, *Angiogenesis Analyzer for ImageJ*, November **2017**, http://image.bio.methods.free.fr/ImageJ/?Angiogenesis-Analyzer-for-ImageJ#nb1.
[35] N. Xue, S. Khodaparast, L. Zhu, J. K. Nunes, H. Kim, H. A. Stone, *Nat. Commun.* **2017**, *8*, 1960.
[36] J. Barthes, H. Ozcelik, M. Hindie, A. Ndreu-Halili, A. Hasan, N. E. Vrana, *BioMed Res. Int.* **2014**, *2014*, 1.
[37] J. Thumbs, H.-H. Kohler, *Chem. Phys.* **1996**, *208*, 9.
[38] H. Treml, S. Woelki, H.-H. Kohler, *Chem. Phys.* **2003**, *293*, 341.
[39] S. Stokols, M. H. Tuszynski, *Biomaterials* **2004**, *25*, 5839.
[40] J. C. Crocker, D. G. Grier, *Phys. Rev. Lett.* **1996**, *77*, 1897.
[41] Y. Jing, J. Jing, L. Ye, X. Liu, S. E. Harris, R. J. Hinton, J. Q. Feng, *Sci. Rep.* **2017**, *7*, 10020.
[42] R. F. Canadas, J. M. Oliveira, A. P. Marques, R. L. Reis, *Multi-chambers bioreactor, methods and uses, Patent WO2016042533A1* **2018**.
[43] R. F. Canadas, J. M. Oliveira, A. P. Marques, R. L. Reis, *Rotational dual chamber bioreactor: methods and uses thereof, Patent WO2014141136A1* **2014**.
[44] M. A. J. Finnilä, J. Thevenot, O. Aho, V. Tiitu, J. Rautiainen, S. Kauppinen, M. T. Nieminen, K. Pritzker, M. Valkealahti, P. Lehenkari, S. Saarakkala, *J. Orthop. Res.* **2017**, *35*, 785.
[45] H. Lin, T. P. Lozito, P. G. Alexander, R. Gottardi, R. S. Tuan, *Mol. Pharmaceutics* **2014**, *11*, 2203.
[46] M. Saito, T. Sasho, S. Yamaguchi, N. Ikegawa, R. Akagi, Y. Muramatsu, S. Mukoyama, N. Ochiai, J. Nakamura, K. Nakagawa, A. Nakajima, K. Takahashi, *Osteoarthritis Cartilage* **2012**, *20*, 1574.
[47] C. Correia, W. L. Grayson, M. Park, D. Hutton, B. Zhou, X. E. Guo, L. Niklason, R. A. Sousa, R. L. Reis, G. Vunjak-Novakovic, *PLoS One* **2011**, *6*, e28352.
[48] U. H. Langen, M. E. Pitulescu, J. M. Kim, R. Enriquez-Gasca, K. K. Sivaraj, A. P. Kusumbe, A. Singh, J. Di Russo, M. G. Bixel, B. Zhou, L. Sorokin, J. M. Vaquerizas, R. H. Adams, *Nat. Cell Biol.* **2017**, *19*, 189.
[49] E. A. Bayer, M. V Fedorchak, S. R. Little, *Tissue Eng., Part A* **2016**, *22*, 1296.
[50] S. K. Ramasamy, A. P. Kusumbe, T. Itkin, S. Gur-Cohen, T. Lapidot, R. H. Adams, *Annu. Rev. Cell Dev. Biol.* **2016**, *32*, 649.
[51] M. R. Boscariol, A. J. Moreira, R. D. Mansano, I. S. Kikuchi, T. J. A. Pinto, *Int. J. Pharm.* **2008**, *353*, 170.
[52] J. Schindelin, I. Arganda-Carreras, E. Frise, V. Kaynig, M. Longair, T. Pietzsch, S. Preibisch, C. Rueden, S. Saalfeld, B. Schmid, J.-Y. Tinevez, D. J. White, V. Hartenstein, K. Eliceiri, P. Tomancak, A. Cardona, *Nat. Methods* **2012**, *9*, 676.